Arch. Mech., **70**, 5, pp. 457–480, Warszawa 2018, DOI: 10.24423/aom.2965
SEVENTY YEARS OF THE ARCHIVES OF MECHANICS

Experimental study of the flow around two finite square cylinders

A. SOHANKAR[1)], M. ABBASI[1)], M. NILI-AHMADABADI[1)],
MD. MAHBUB ALAM[2)], F. ZAFAR[2)]

[1)] *Department of Mechanical Engineering
Isfahan University of Technology
Isfahan, 84156-83111, Iran*

[2)] *Institute for Turbulence-Noise-Vibration Interaction and Control
Harbin Institute of Technology, Shenzhen
Shenzhen 518055, China
e-mails: alamm28@yahoo.com; alam@hit.edu.cn*

An experimental investigation is conducted on the air flow past two wall-mounted finite length side-by-side square cylinders, each of the aspect ratio $AR = 7$. The cylinder center-to-center spacing ratio T/d is varied from 2 to 6, where d is the side-width of the cylinder. The cylinders are placed at three incidence angles with respect to the freestream velocity, i.e. both cylinders at zero incidence angle (case I), both cylinders at 45° incidence angle (case II), and one cylinder at zero incidence angle with the other at 45° incidence angle (case III). The pressure distributions on the surfaces of the cylinders are measured at Reynolds numbers of 5.9×10^4–8.1×10^4. In addition, the flow structures are visualized in a smoke wind tunnel at the Reynolds number of 2×10^3. Depending on the flow characteristics, four flow structures are identified at the mid-height of the cylinders, namely the asymmetric flow, antiphase shedding flow, leading-edge separated flow and wedge flow. The sectional drag near the bottom is more sensitive to T/d than that near the top. The sectional drag coefficient measured at $0.5d$ below the mid-span can represent the surface-averaged drag coefficient on the entire cylinder.

Key words: experimental study, pressure coefficient, drag coefficient, wall-mounted finite square cylinders, angle of incidence, side-by-side arrangement.

1. Introduction

There are many applications of the flow over rectangular or circular bluff bodies in a group. Some examples are tall buildings, tubes in heat exchangers, bridges, chimneys, offshore platforms, and chemical reaction towers. In spite of their simple geometry, the flow around these models contains features, such as flow separation and reattachment, wake, shear layer instability, interaction between shear layers, vortex shedding, vortex impingement, separation bubble, etc. Recently, the study of this flow has become an area of interest for many researchers.

Many attempts have been undertaken to study the flow across a single two-dimensional (infinite) square or circular cylinder. Attention has been paid to examining the flow over infinite (two-dimensional) square cylinders in side-by-side arrangements at the zero incidence angle for different Reynolds numbers (Re) and spacing ratio T/d, where T is the cylinder center-to-center spacing and d is the cylinder side-width. For two infinite square cylinders, an increase in T/d results in the asymmetric flow (T/d = 1.2–2.2) and coupled vortex shedding flow ($2.2 < T/d < 5$) [1]. In the case of asymmetric flow, the wake behind the cylinders is asymmetric, where the gap flow is biased toward a cylinder, forming a narrow and a wide wake behind the cylinders, respectively [1]. The coupled vortex shedding flow is also known as the 'synchronized' flow, where the vortex shedding from the cylinders occurs in an inphase or antiphase fashion. The wake of two infinite square cylinders in side-by-side was investigated in detail based on flow visualization at $Re = 300$ by Alam and Zhou [2]. Their experiments were carried out for T/d = 1.0–5.0. They classified the flow patterns into four based on T/d. The single bluff body regime ($T/d < 1.2$): flow through the gap is too feeble to split the wake into two streets, hence a single large wake forms behind the cylinders. The asymmetric wake regime ($1.2 < T/d < 2.1$): the gap flow splits the wake into one narrow and one wide wake. The transition regime ($2.1 < T/d < 2.4$): asymmetric wake flow and the coupled street flow intermittently appear. The coupled street regime (T/d = 2.4–5.0): the two streets are coupled in inphase or antiphase modes.

Some experimental and numerical studies have been performed on the flow over a single surface-mounted finite circular [3] or square [4] cylinder. As expected, there are some similarities/dissimilarities of the flow features between an infinite and a finite (wall-mounted) cylinder. The local flow (tip vortex) close to the free end and the cylinder-wall junction flow (base vortex) are the main differences, which can provide a complicated and three-dimensional wake flow for the wall-mounted cylinder. The formation of vortex shedding from the sides of a wall-mounted tall cylinder is a similarity between these two configurations. In addition to Re, the cylinder aspect ratio AR, incidence angle α, and wall boundary layer thickness relative to the cylinder height, the flow over side-by-side cylinders is strongly influenced by T/d. Thus, the aforementioned complexities increase when the flow over two wall-mounted cylinders is considered. Despite its great relevance to engineering applications, the flow around two wall-mounted cylinders has received much less attention than that around the infinite cylinders.

The effect of α on the flow around a single finite square cylinder has not been extensively studied in the literature. The combined effects of α and AR for the flow past a single finite square cylinder have received relatively little attention [5, 6]. To the authors' knowledge, no research results have been reported on the flow over two wall-mounted finite square cylinders in side-by-side arrangements. The aim of the present work is to study the flow for this configuration. The focus is on the effects of α and T/d on the flow structures. Pressure measurement and smoke flow visualization experiments are conducted at $Re = (5.9–8.1) \times 10^4$ and 2×10^3, respectively. The T/d is varied from 2 to 6. Following the definitions of incidence angles α_1 and α_2 (Fig. 1), three configurations are examined, i.e. case I: $\alpha_1 = \alpha_2 = 0°$, case II: $\alpha_1 = \alpha_2 = 45°$, case III: $\alpha_1 = 45°$, $\alpha_2 = 0°$.

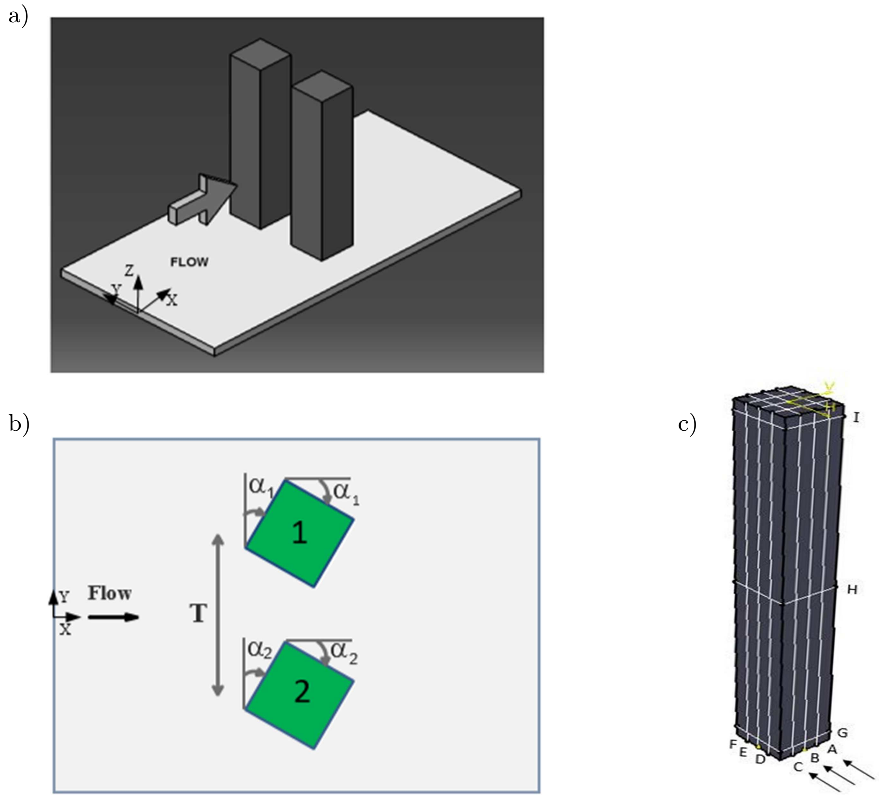

FIG. 1. Schematic view of two wall-mounted finite square cylinders in side-by-side arrangement; a) three-dimensional view, b) top view, c) belts (A to I) defined for illustrating pressure measurements on the cylinder surfaces.

For a single cylinder, asymmetric Karman vortex shedding is absent at a low AR while it appears at a higher AR, e.g. $AR = 7$. Thus, interactions are possible of the base vortices, tip vortices and Karman vortices at $AR = 7$ that represents a more generalized configuration. In reality, the flow over a structure (cylinder) undergoes various Reynolds numbers depending on the structure size and approaching flow velocity. In addition, the major flow physics does not change much when $Re > 10^3$ [7, 8, 9]. However, this may or may not be the case when two cylinders interact with each other. We have thus considered a range of $Re = 2 \times 10^3$–8.1×10^4.

2. Experimental details

2.1. Pressure measurement

The pressure measurement experiment was carried out in an open-circuit wind tunnel with a test section of 200 cm in length, 90 cm in width, and 90 cm in height (Fig. 2). The freestream velocity was varied as 18 m/s, 21 m/s and 25 m/s, corresponding to $Re = 59\times10^3$, 68×10^3, and 81×10^3, respectively, where the Re is based on the incoming velocity U and d. The freestream turbulence intensity was less than 0.3% for the velocity range. The non-uniformity of the flow velocity across the test section was less than 0.7%. Figure 1 shows the schematic view of the problem under consideration. The incidence angles (α_1, α_2) of the two cylinders are also shown in the figure. In addition, the belts (A to I) in Fig. 1c) illustrate the pressure measurement points on the cylinder surfaces. A rectangular Cartesian coordinate system (x, y, z) is adopted to describe the flow, in which the x-axis is aligned with the streamwise flow direction, the z-axis is in the wall-normal direction, and the y-axis is in the cross-stream direction, see Fig. 1. The front and rear surfaces of the cylinders at $\alpha_1 = \alpha_2 = 0°$ are parallel to the y-z plane.

Three-dimensional models were made of Plexiglas, with dimensions $5\,\text{cm} \times 5\,\text{cm} \times 35\,\text{cm}$ corresponding to $AR = 7$. The models were installed on the horizontal floor at a distance of about 100 cm from the leading edge of the test section. The boundary layer thickness δ at this position is about 25 mm ($\delta/h = 0.07$, where h is the cylinder height) based on the direct measurement of velocity profile on the floor. In addition, based on empirical correlations for turbulent flat plate boundary layer [10], the boundary layer thickness, momentum thickness, and the shape-factor at this position for $Re = 81 \times 10^3$ or $Re_x = 1.62 \times 10^6$ are about 21.9 mm, 2.1 mm and 1.29, respectively, yielding $\delta/h = 0.06$. This value agrees with that measured directly.

The local surface pressure was measured from the taps on the cylinders. The pressure taps were distributed on the surfaces (along the belts) of each model. All taps were connected to the pressure box with 1-mm diameter tubes. The pressure box had 32 channels with Honeywell sensors, connected to a computer for data acquisition. The surface pressure coefficient was computed as $C_P = (p - p_\infty)/0.5\rho U^2$, where U is the freestream velocity, p_∞ is the freestream static pressure, P is the pressure measured at pressure tap, and ρ is the fluid density.

The drag coefficient C_d was determined as $C_d = 2F_d/(\rho U^2 A)$, where F_d is the drag force estimated from pressure distributions on the cylinder surface, and $A = hd(\sin\alpha + \cos\alpha)$ is the cylinder projected area normal to the flow. At $\alpha = 0°$ and $45°$, $A = hd$ and $A = \sqrt{2}\,hd$, respectively. Similarly, the sectional drag coefficient C_D was estimated as $C_D = 2F_D/(\rho U^2 \acute{A})$, where F_D is the drag force at a sectional height z, and $\acute{A} = d(\sin\alpha + \cos\alpha)$.

About 20 000 samples were recorded with a sampling frequency of 1 kHz for each pressure tap, the sampling time being 20 s. In order to see whether the sampling time was long enough, the sampling time was varied as 10, 15, 20 and 30 s, and the results show that the variation in C_d between the sampling time 10 and 20 s was less than 1%. Based on the standard deviation of the number of data collected from repeated measurements, the uncertainty in C_d measurement is estimated to be less than 5%.

2.2. Smoke visualization

A low-speed vertical smoke tunnel was used to visualize the flow structure around the models (Fig. 2). The operating freestream velocity U in the test-section is adjustable between 1.5 and 5 m/s by an electronic inverter. The maximum turbulence intensity is less than 0.85% for $U > 2$ m/s. The smoke tunnel had a test section height, width, and length of 18, 10 and 24 cm, respectively. The models with a side width of 1 cm and an aspect ratio of 7, constructed from

a) b)

FIG. 2. a) Smoke tunnel, and b) open-loop wind tunnel.

steel, are employed. The $U = 3$ m/s was chosen, corresponding to $Re = 2 \times 10^3$. The vaporized kerosene is piped into a strut located directly upstream of the test section. A series of equally spaced holes at the trailing edge of the smoke strut introduce smoke filaments into the flow. The movement of the smoke-lines is captured with a high-speed camera at a rate of 4000 frames/s.

The smoke visualization was performed at the moderate $Re = 2 \times 10^3$, smaller than the pressure measurement Reynolds numbers. This is done because the smoke filaments are less dissipated at a low Re, which gives a reasonably clear picture of the flow. Although the Re employed is lower for the flow visualization than for the pressure measurement, but it is expected that the major features are qualitatively the same at the two Re ranges [1, 2, 7, 11–13].

3. Results and discussion

3.1. Flow structures

Figures 3–5 show snapshots of smoke flow structures at some representative T/d for the different α_1 and α_2 considered. It should be noted that the smoke visualization data are provided for the x-y plane at the cylinder mid-height ($z/d = 3.5$). In addition, the flow over the free end is also visualized for case I (Fig. 6). As mentioned in the introduction, four flow regimes were reported for two side-by-side infinite cylinders [1]. Some of these regimes are also qualitatively observed for the x-z plane at the cylinder mid-height ($z/d = 3.5$) wall-mounted cylinders in this work as they are discussed in this section.

Figure 3 shows flow patterns for various T/d for case I ($\alpha_1 = \alpha_2 = 0°$). At $T/d = 2.0$, the gap flow between two cylinders producing a jet-like flow is biased toward one of the cylinders, forming a narrow and a wide wake (Fig. 3a, b). The flow structures at two different instants display similarities to some extent. In addition, dissimilarities are observed in the size of the narrow and wide wake flows between the two instants (Fig. 3a, b), suggesting that the flow is time-dependent.

Figures 3c, d show, respectively, the flow patterns for $T/d = 3$ and 4, where the gap flow is straight, and vortex shedding from the cylinders occurs in an antiphase mode. For these T/d, the wake of a cylinder is similar to that of the other. An inphase flow pattern was also reported for infinite cylinders at $T/d = 3$ and 4 [1, 2]. The inphase flow pattern was, however, not observed for finite cylinders at these T/d considered. For the finite cylinders, the tip vortices play a role in the wake. Thus, the tip vortices from the two cylinders might be responsible for the absence of the inphase flow.

Figure 4 shows flow patterns for the case II ($\alpha_1 = \alpha_2 = 45°$). The upstream flow over the windward of the cylinders is symmetric. The flow separations occur

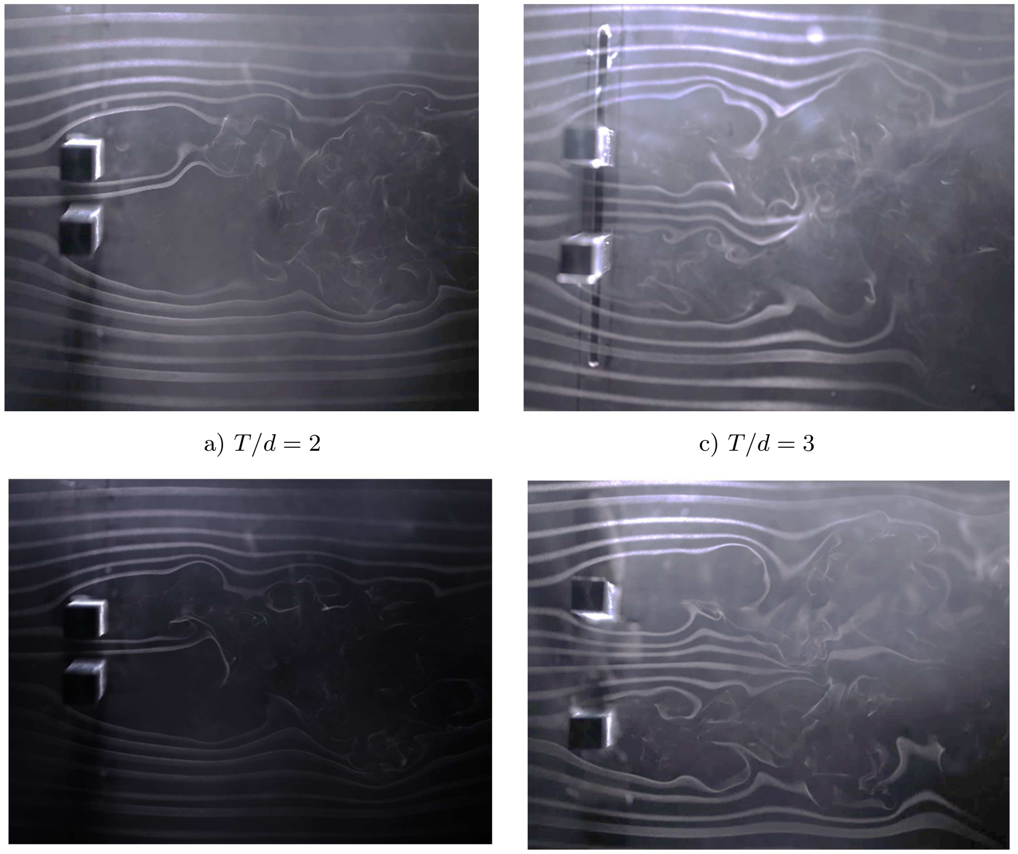

a) $T/d = 2$ c) $T/d = 3$

b) $T/d = 2$ d) $T/d = 4$

FIG. 3. Flow patterns obtained from smoke flow visualization in the x-y plane at the cylinder mid-height ($z/d = 3.5$) for case I ($\alpha_1 = \alpha_2 = 0°$); a) $T/d = 2$ (instant t1), b) $T/d = 2$ (instant t2), c) $T/d = 3$, d) $T/d = 4$.

at the two sharp edges of the cylinders, and the lateral size of the wake is larger than that for the case I (Fig. 3). The flow pattern for $T/d = 2$ (Fig. 4a) is similar to that for the case I, where the gap flow deviates to one of the cylinders. For $T/d = 3$ and 4 (Fig. 4b, c), an antiphase vortex shedding prevails, and the separated flow structures are similar to those of the case I in Fig. 3. To the best of the authors' knowledge, no results have been reported for the flow over side-by-side wall-mounted square cylinders at $\alpha_1 = \alpha_2 = 45°$. Thus, the flow around a single infinite cylinder at $\alpha = 45°$ is provided in Fig. 4d for $Re = 2 \times 10^4$ [11]. This flow pattern is identified as a wedge flow mode. There are some similarities between the patterns in Figs. 4c and 4d especially for the outer sides. It should be noted that three or four flow modes were reported for an infinite single cylinder, depending on α and *Re*. For example, three flow modes were identified depending on $\alpha = 0°–45°$ [11, 12]. The leading-edge separation mode (complete separation) without reattachment occurs at small α ($< 10°$). The separation bubble mode takes place at intermediate α where the flow separating from the leading corner reattaches on the lower surface, which leads to a separation bubble occurring on the lower surface. The wedge flow or boundary-layer-attached flow prevails at α close to 45°, where the flow remains attached on the windward surfaces. Here, the leading-edge separation and wedge flow modes are observed for finite cylinders (Figs. 4 and 5).

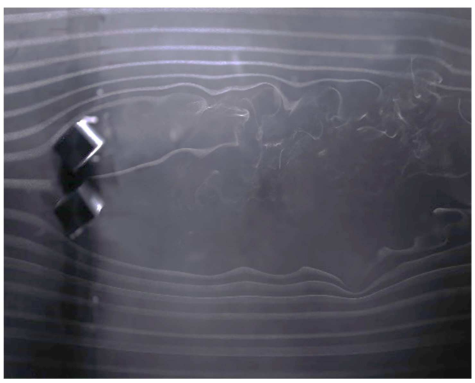

a) $T/d = 2$

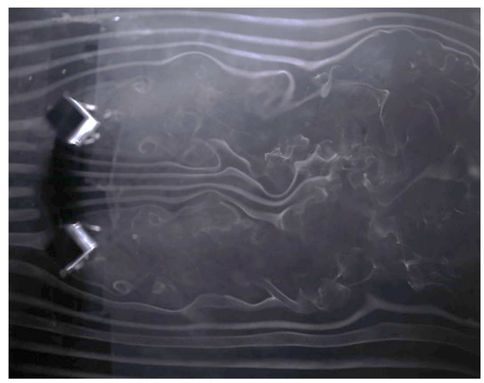

c) $T/d = 4$

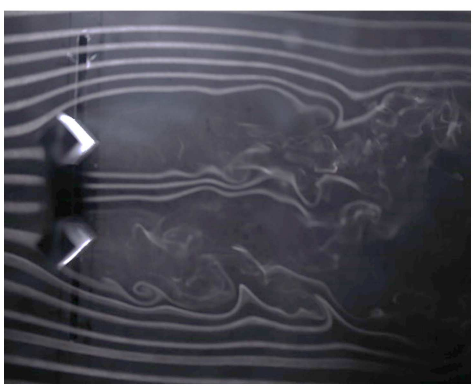

b) $T/d = 3$

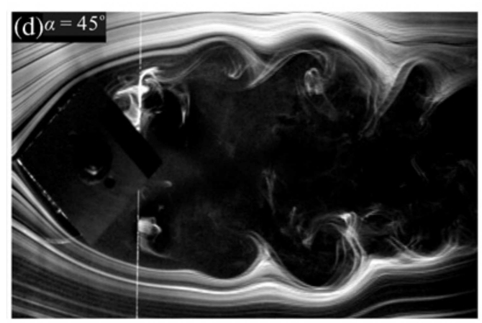

d) Single cylinder

FIG. 4. Visualized flow patterns around the side-by-side wall-mounted cylinders in the x-y plane at the cylinder mid-height ($z/d = 3.5$) for case II ($\alpha_1 = \alpha_2 = 45°$); a) $T/d = 2$, b) $T/d = 3$, c) $T/d = 4$, d) single infinite cylinder at $\alpha = 45°$ [11].

Figure 5 shows the flow patterns for the case II ($\alpha_1 = 0°$, $\alpha_2 = 45°$). For $T/d = 2$ (Fig. 5a), the flow passing through the gap deviates toward the cylinder

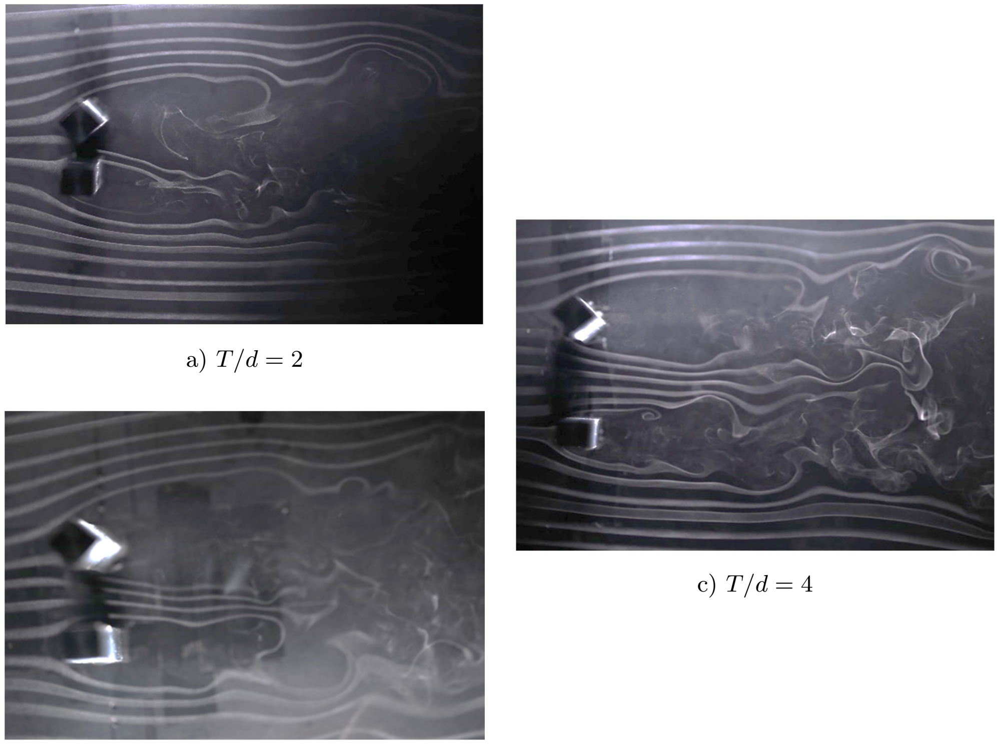

a) $T/d = 2$

b) $T/d = 3$

c) $T/d = 4$

FIG. 5. Visualized flow patterns in the x-y plane at the cylinder mid-height ($z/d = 3.5$) for case III ($\alpha_1 = 0°$, $\alpha_2 = 45°$); a) $T/d = 2$, b) $T/d = 3$, c) $T/d = 4$.

of $\alpha_1 = 0°$ for all the time. As explained regarding Figs. 3a, b and 4a for $T/d = 2$ (cases I, II), the gap flow can be biased toward either of the cylinders, similar to those reported for infinite cylinders for $T/d < 2.1$ [2]. For the case III, the flow between the two cylinders is also accelerated, producing a jet-like flow and asymmetric wake, where the wide and narrow wakes prevail all the time behind the cylinders with $\alpha_2 = 45°$ and $\alpha_1 = 0°$, respectively. This new pattern occurs due to the asymmetry of the geometry with respect to incident flow. A similar pattern is observed for $T/d = 3$ (Fig. 5b) but with a smaller deviation of the gap flow in comparison with that of $T/d = 2$ in Fig. 5a. The deviation of the jet flow for $T/d = 4$ is minimal but the two wakes are still different in size because of the different projected widths of cylinders normal to the flow direction.

As concluding remarks, (i) asymmetric and antiphase shedding flows are identified for two side-by-side cylinders while leading-edge separated flow and wedge flow are observed for the individual cylinders; (ii) asymmetric and antiphase flows emerge at $T/d = 2$ and 3-4, respectively, for cases I and II, while only

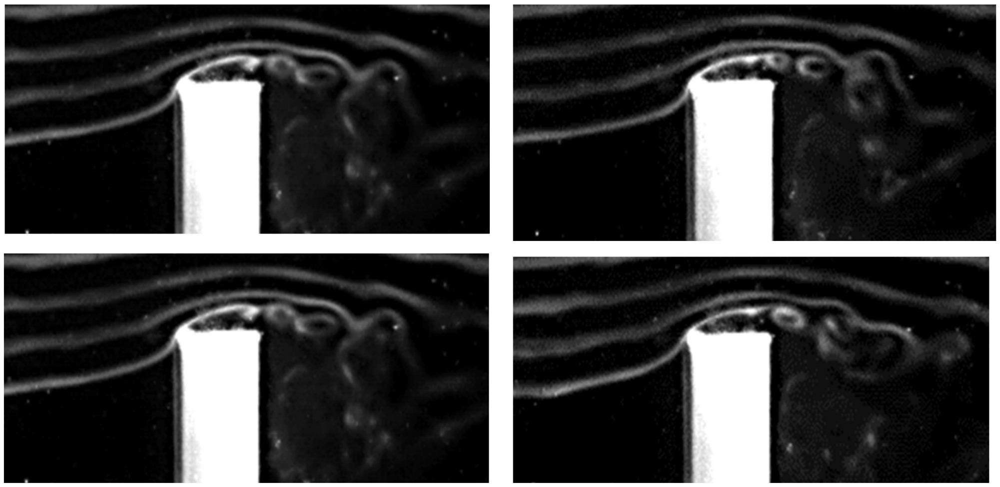

Fig. 6. Visualized flow close to the free end of a cylinder for case I at four selected time instants.

asymmetric flow appears for the case III; (iii) for the asymmetric flow, the gap flow is unstable, may switch from a side to the other for cases I and II, but it is stable for the case III, biased only toward the cylinder with $\alpha = 0°$.

One of the main differences in flow features between infinite and finite cylinders is the occurrence of the tip vortices from the free end for the finite cylinder case, which generates a downwash flow making the wake flow more complicated. Figure 6 shows the flow pattern over the free end of one of the cylinders at four instants for the case I. The flow separates from the leading edge of the free end and produces Kelvin–Helmholtz (KH) vortices in the shear layer. The separated shear layer is laminar for a small length close to the separation point.

3.2. Surface pressure and drag coefficients

The time-mean pressure coefficient C_P distributions on the cylinder surface (along the nine belts denoted as A to I in Fig. 1c) are presented in Figs. 7–12. The pressure measurements were carried out at $Re = 5.9 \times 10^4$, 6.8×10^4, and 8.1×10^4. The belts crossing the four edges of each cylinder are labeled with the numbers 1 to 4 for the cylinder 1 (Fig. 1) and 5 to 8 for the cylinder 2, for example (Fig. 7). The distance along the belts is denoted with a variable S, e.g. see Fig. 7. The C_P results are presented on two types of belts. The first type is in the x-y plane, $0.3d$ away from the wall (G), at the mid-height ($h/2$), and $0.2d$ away from the free end (I) of the cylinders (Fig. 1). The belts (A, B and C) in the second type are in the x-z plane ($\alpha_1 = \alpha_2 = 0°$), $0.15d$, $0.5d$ and $0.85d$ away from one of the vertical edges of the front surface (Fig. 1). Similarly, belts D, E, and F appearing in the y-z plane ($\alpha_1 = \alpha_2 = 0°$) are $0.15d$, $0.5d$ and $0.85d$ away from the leading vertical edge of the side surface, see Fig. 1c. In the case of a cylinder at $\alpha = 45°$, all the vertical surfaces have a 45° inclination to the freestream flow. In fact, two lateral surfaces of the cylinders are located on the windward side, while the other two surfaces are on the leeward side in the wake region. In contrast to the cylinder at $\alpha = 0°$, the belts of A, B, C are similar to those of F, E, D, respectively for cases with $\alpha = 45°$, where the belts A to E are located on the windward, top and leeward surfaces.

Figure 7 shows C_P distributions along the belt H for the case I ($\alpha_1 = \alpha_2 = 0°$) at different T/d. The C_P on the windward surfaces of the two cylinders (H_1–H_2 and H_5–H_6) is positive, about 1.0 at their center (stagnation pressure), regardless of T/d. The flow separates from the edges of the windward surfaces of the cylinders (Fig. 3); the C_P thus reduces largely on the lateral and leeward surfaces. For a given T/d, the C_P does not change much on the leeward surface of either cylinder but varies on the lateral surfaces especially on the inner ones (H_1–H_4 and H_5–H_8), the variation being lager for smaller T/d (e.g. $T/d = 2$, 3). As mentioned previously from Fig. 3, the asymmetric flow is generated at a low T/d while the coupled-vortex shedding flow emerges at a large T/d. As in Fig. 3, the flow structure at $T/d = 2$ is different from that at $T/d = 3$, the inner shear layers are closer to side surfaces at $T/d = 2$ than $T/d = 3$. The difference results in a large variation in C_P on the inner side surface (H_1–H_4 and H_5–H_8) for the former T/d (Fig. 7). In fact, the formation of the jet-like flow between two inner surfaces (H_1–H_4 and H_5–H_8) for a low T/d is the main reason for differentiating C_P on the inner side surfaces. In general, C_P distributions along the belt H for the two cylinders are similar to each other. As reported for infinite cylinders [1, 2, 13], the similarity between the C_P distribution of a finite cylinder in a two-cylinder arrangement and that of a single finite cylinder become complete at a higher T/d where the flow interference between the two cylinders is small, and the flow over each cylinder approximately approaches that of a single cylinder.

Figure 8 shows the variation in C_P along belts G (near the floor) and I (close to the free end). As observed in Fig. 7 for the belt H, the results for the two cylinders are similar to each other, especially for a large T/d. The same was also observed for belts G and I, thus the results in Fig. 8 are presented for cylinder 1 only to avoid repeating similar figures. Qualitatively similar variations are observed for the results at the three belts if one compares Figs. 7 and 8. The similarity is more remarkable for the belts H and I, while the discrepancy between the results for belts G and H becomes higher due to the wall effect and its upwash flow on the wake structure. In fact, the interactions of the upwash flow close to the wall, vortex shedding, and downwash flow from the tip together with the gap flow are the main reasons for the aforementioned variations.

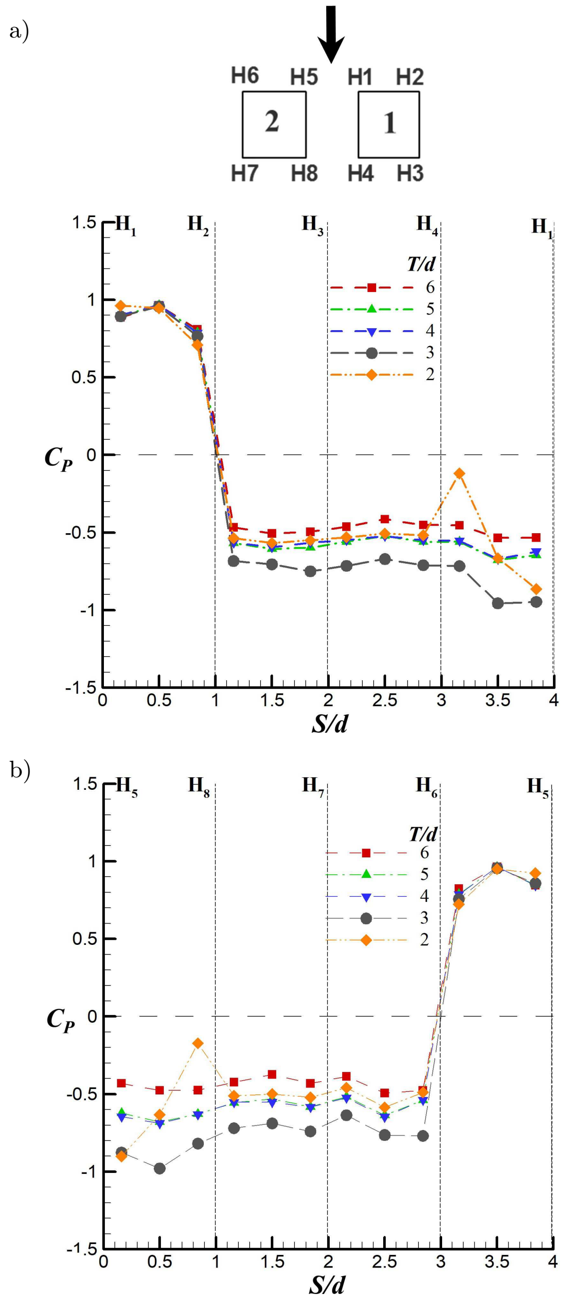

Fig. 7. Time-mean pressure coefficient along the belt H for case I ($\alpha_1 = \alpha_2 = 0°$); a) cylinder 1, and b) cylinder 2, $Re = 8.1 \times 10^4$.

Figures 9 and 10 show C_P distributions along belts A, B, C and belts D, E, F, respectively, for the case I ($\alpha_1 = \alpha_2 = 0°$). Recall that the parallel belts A, B,

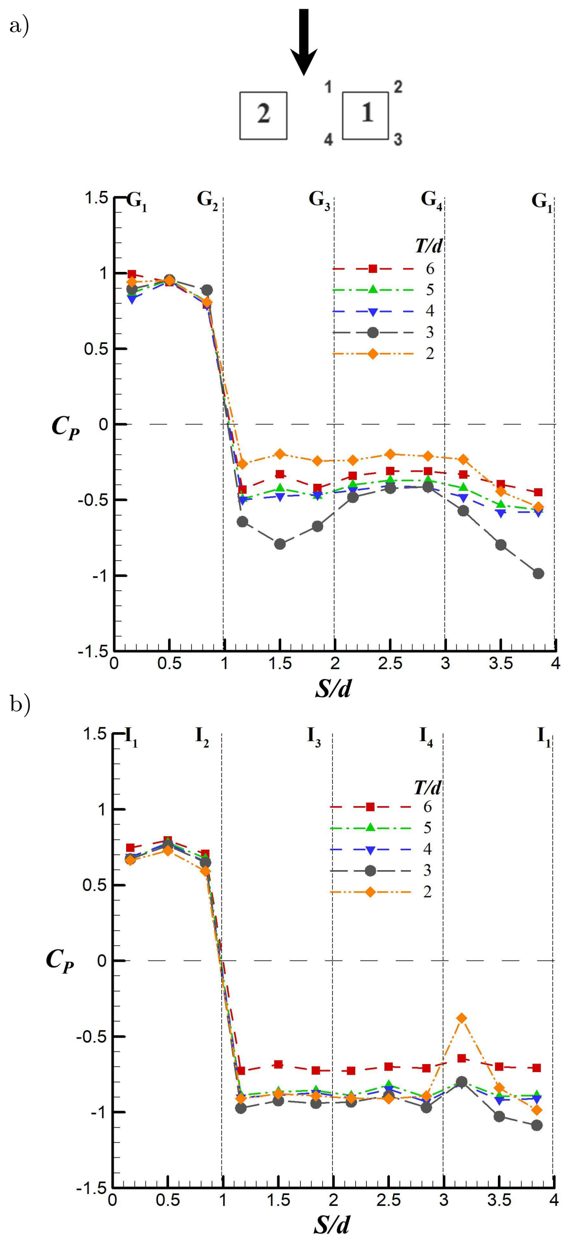

Fig. 8. Time-mean pressure coefficient along: a) belt G and b) belt I of cylinder 1. Case I ($\alpha_1 = \alpha_2 = 0°$), $Re = 8.1 \times 10^4$.

and C are on the windward, top and leeward surfaces of the cylinder while the parallel belts D, E, F are on the outer side, top and inner side surfaces (Fig. 1).

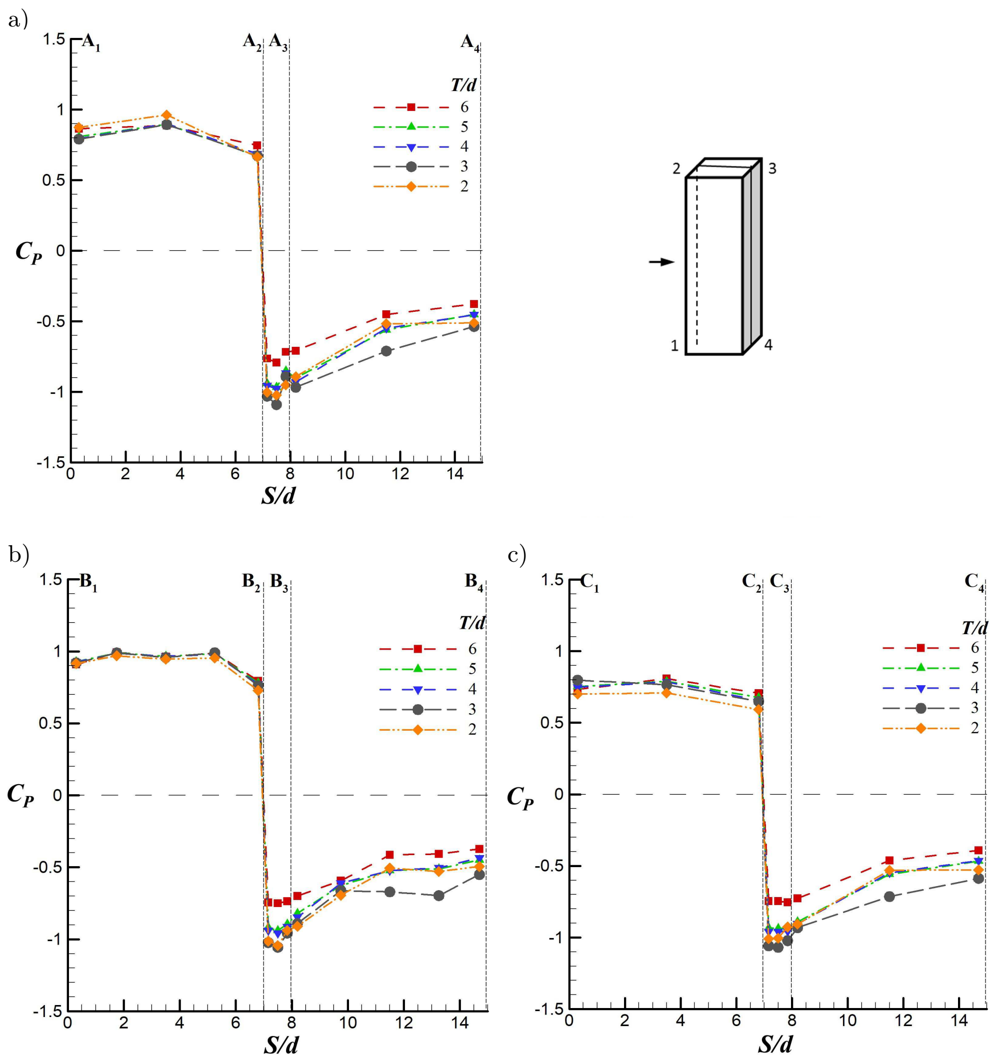

Fig. 9. Time-mean pressure coefficient along: a) belt A, b) belt B, c) belt C, of the cylinder 1 for case I ($\alpha_1 = \alpha_2 = 0°$), $Re = 8.1 \times 10^4$.

Due to a similarity between the results of two cylinders as discussed previously, the results are presented for cylinder 1 only in Figs. 9 and 10.

The results on belts A, B, and C have a similar trend while they are quantitatively different from each other (Fig. 9). On the front surface (windward) of the cylinder (e.g. B_1–B_2), C_P is positive, not much dependent on T/d, especially for the belt B. The flow separating from the leading edge (A_2–B_2–C_2) of the top surface causes a large reduction in C_P (negative values). The T/d has a significant effect on C_P on the top surface, C_P magnitude getting higher

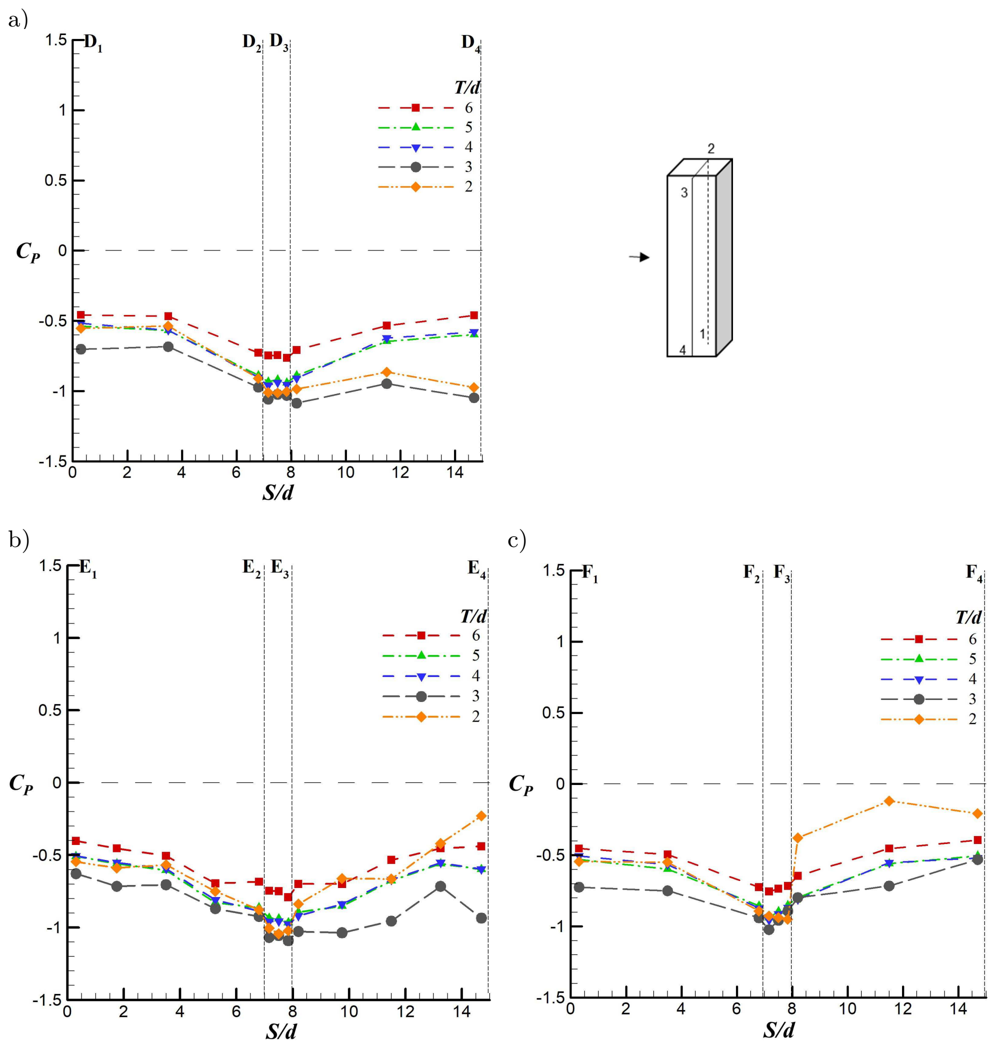

FIG. 10. Time-mean pressure coefficient along: a) belt D, b) belt E, c) belt F, of cylinder 1 for case I ($\alpha_1 = \alpha_2 = 0°$), $Re = 8.1 \times 10^4$.

at a smaller T/d. At the leeward side of the cylinder, C_P increases along the cylinder height from the top to the bottom. The wake, downwash flow from the free end, and upwash flow from the wall are the main reasons for this behavior on the leeward side. Again similar to the results on the cylinder top, C_P varies as T/d changes from 2 to 6.

Figure 10 shows C_P distributions along belts D, E, and F of the cylinder 1. These belts are on the outer side, top, and inner side surfaces, all lying in the separated regions. The C_P along the entire length of a belt is thus negative.

On the outer side surface (e.g. line E_1–E_2 of belt E), the C_P gradually decays, becoming more negative, for all T/d examined when one moves from the first point close to the wall to the last point near the top. A similar trend is observed on the inner side surfaces. Due to the flow interference on the inner side surfaces, an asymmetry is observed between the results on the inner and outer side surfaces, especially for small T/d, i.e. $T/d = 2$, and 3. At high T/d $(= 4, 5, 6)$, the flow interference weakens and the results on the inner and outer sides become approximately similar. The minimum C_P on these belts (D, E, F) occurs on the cylinder top (e.g. line E_2–E_3 of belt E) due to a strong recirculation of the separated flow (Fig. 6).

The drag coefficient C_d for various T/d is presented in Table 1. A comparison of the present results with those for side-by-side infinite cylinders and a single wall-mounted cylinder is also made in the table [13–18]. No results for side-by-side finite cylinders were found in the literature. Before comparing the results, two points should be noted. Firstly, the most of the reported C_d in Table 1 are the sum of the pressure and frictional forces, while our results are due to the pressure force only. Secondly, for a sharp-edged bluff body at a high *Re*, the friction drag force is very small compared to the pressure force. Thus, the pressure drag coefficient would be very close to the total drag coefficient.

As seen in Table 1, the C_d of the two cylinders is not the same for $T/d = 2$ due to the formation of the narrow and wide wakes (Fig. 3). Such a difference was also reported for infinite cylinders [13, 18], see also Table 1. At a higher T/d, the two cylinders have the same C_d. The effect of the flow interference between the cylinders weakens with T/d increasing. Hence, the C_d of each cylinder approaches that of a single wall-mounted cylinder (Table 1). The difference in C_d between the cylinder 1 in the present study ($Re = 8 \times 10^4$, $AR = 7$, $T/d = 6$) and single cylinder [14, 15] is less than 5%. From the table, it is also found that the *Re* has a negligible effect on the results as reported for a single cylinder [9]. As seen in Table 1, the C_d of the finite wall-mounted cylinders is about 35% lower than that of infinite cylinders [13, 18]. The main reason for this reduction is the formation of a longer longitudinal reverse flow zone for the finite cylinders. The reduction is attributed to (i) an increased momentum in wake due to downwash and upwash flows from the free end and the floor, respectively, and (ii) the formation of the turbulent boundary layer on the floor.

Figure 11 shows the sectional drag coefficient ratio C_D/C_d (scaled with the corresponding total surface-average drag coefficient C_d) for various T/d along the cylinder height z/d. The trend of C_D/C_d variation is similar for various T/d except for $T/d = 3$. While C_D/C_d has a local maximum at $z/d = 5$ for $T/d = 3$, it becomes maximum near the bottom wall ($z/d = 0.5$) for the other T/d. The different trait for $T/d = 3$ was also observed in Table 1 and Figs. 7–10, where $T/d = 3$ corresponded to a higher C_d (Table 1) and more negative pressure on

Table 1. Comparison of C_d for various configurations, i.e. SBS-WM (wall-mounted finite length side-by-side cylinders, case I: $\alpha_1 = \alpha_2 = 0°$), single-WM (single wall-mounted finite length cylinder), SBS-INF (infinite side-by-side cylinders).

Configurations	T/d	AR	Re	C_d	
				Cyl 1	Cyl 2
SBS-WM (present)	2	7	8.1×10^4	1.32	1.44
SBS-WM (present)	3	7	8.1×10^4	1.54	1.52
SBS-WM (present)	4	7	8.1×10^4	1.44	1.44
SBS-WM (present)	5	7	8.1×10^4	1.45	1.45
SBS-WM (present)	6	7	8.1×10^4	1.34	1.34
Single-WM (Exp. [14])	–	6	1.2×10^4	–	1.41
Single-WM (Exp. [15])	–	3	7.3×10^4	–	1.29
Single-WM (Exp. [15])	–	7	7.3×10^4	–	1.4
Single-WM (Exp. [15])	–	11	7.3×10^4	–	1.46
Single-WM (Exp. [16])	–	18	4.04×10^4	–	1.3
Single-WM (Exp. [17])	–	18	4×10^4	–	1.3
SBS-INF (Exp. [18])	1.5	–	2.1×10^4	1.67	1.74
SBS-INF (Num. [13])	1.5	–	2.1×10^4	1.89	1.71
SBS-INF (Exp. [18])	7	–	2.1×10^4	2.08	2.08
SBS-INF (Num. [13])	7	–	2.1×10^4	2.12	2.12

the side and rear surfaces. Based on Fig. 11, it is possible to say that C_D/C_d near the tip is less dependent on T/d than that near the bottom. That is, the tip vortices do not change much with a change in T/d, but the horseshoe and base vortices do. In fact, the interaction of the base, horseshoe and Kármán vortices between the cylinders is expected to be strong near the base of the cylinder. Overall, C_D/C_d is small and large near the tip and base, respectively. In fact, the pressure coefficients on the front and rear of the cylinder at these sections are different (Fig. 8). Regardless of T/d, $C_D/C_d \approx 1.0$ at $z/d = 3$ that is slightly ($0.5d$) below the midsection. In other words, the sectional drag measured at a section slightly below the midsection can represent the total surface-averaged drag on the cylinder.

The results for the case II ($\alpha_1 = \alpha_2 = 45°$) are shown in Fig. 12, again for the cylinder 1 only. The results are provided for belts H and B. It should be noted that belts A to F are now on the windward, top and leeward faces, where two of the side faces can be regarded as the windward faces while the other two side faces appear as the leeward faces. The two windward sides of the models are exposed to the approaching flow and hence experience positive C_P, while the leeward surfaces lying in the wake region undergo negative C_P. For the flow over a single cylinder, the mean flow has symmetry about the line H_1–H_3, where the

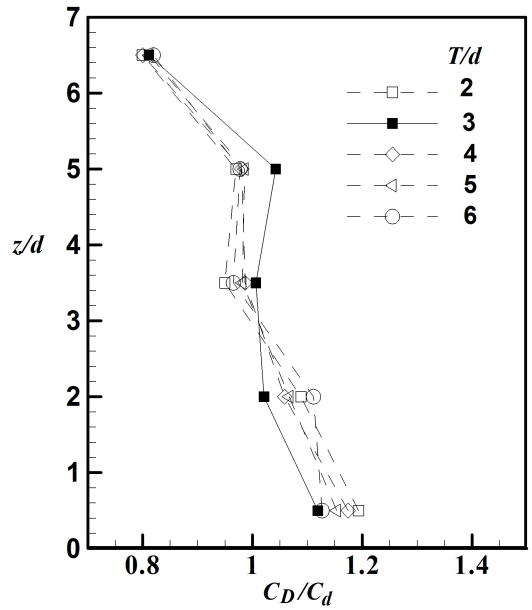

Fig. 11. The sectional drag coefficient ratio C_D/C_d along the cylinder height for case I ($\alpha_1 = \alpha_2 = 0°$); C_D sectional drag coefficient, C_d total surface-averaged drag coefficient.

stagnation point occurs at the vertex H_1. For case II, although the geometry of the cylinders is symmetric, the C_P distribution along the belt H has no symmetry especially for a smaller T/d (Fig. 12a). This asymmetry is caused by the flow interference between the two cylinders. This asymmetry in C_P distribution is large on the front sides (H_1–H_2 and H_1–H_4). When the cylinders are given an incidence angle (cases II and III), the net gap spacing between the edges of the two cylinders reduces/expands in comparison with that with a zero incidence angle (case I). For example, at $T/d = 2$ the net gap spacing ratio is 1 and about 0.6 for cases I and II, respectively. In fact, the net gap spacing for case I remains constant (T/d) along the lateral sides of cylinders, while for the case II it decreases from T/d to $T/d - \sqrt{2}$ and then increases to T/d, the gap acting as a convergent-divergent channel. As such, C_P on the inner-rear surface (H_4–H_3) is more negative than that on the outer-rear surface (H_2–H_3).

Figure 12b shows C_P variations along the belt B of the cylinder 1. For the case II, B_1–B_2 is located at the centerline of one of the windward faces. In fact, it is located on a plane that experiences the approaching flow with a 45° incidence angle. The C_P thus has a value in the order of 0.5. At the edge B_2, the flow separation takes place, and C_P significantly reduces, becoming negative at the top (B_2–B_3). Along B_3–B_4 that is located on one of the leeward faces in the wake region, C_P is negative with a small variation. The C_P value is, however,

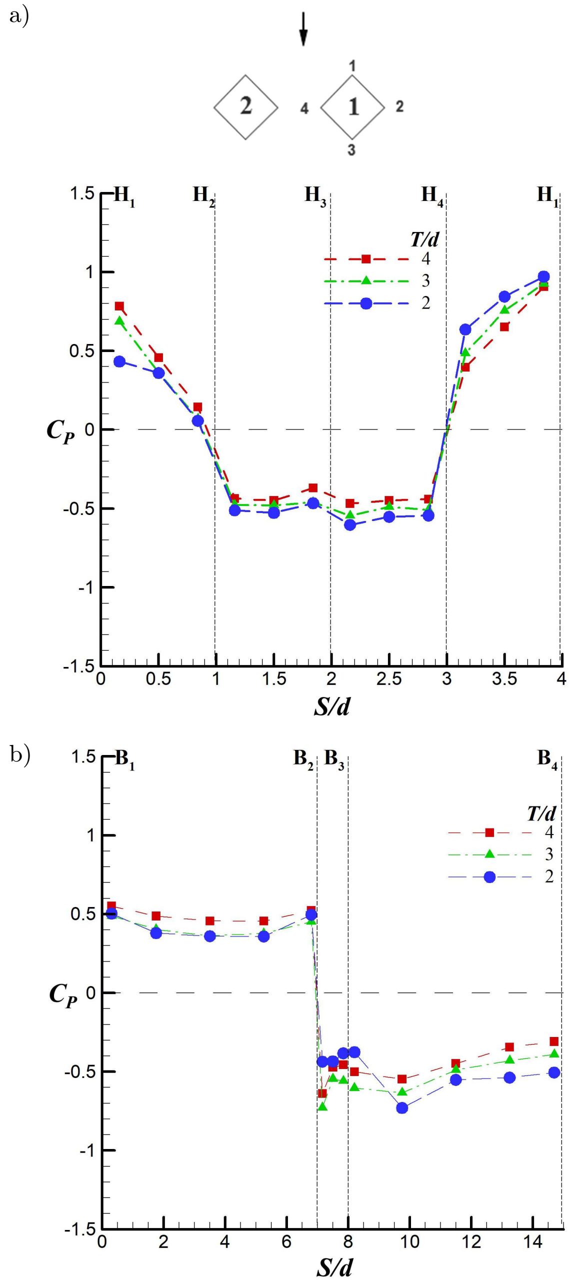

FIG. 12. Time-mean pressure coefficient variation along: a) belt H and b) belt B, of cylinder 1, for case II ($\alpha_1 = \alpha_2 = 45°$), $Re = 8.1 \times 10^4$.

dependent on T/d. For example, the minimum C_P occurs on the top for $T/d = 3$ and 4 while on the leeward face of the cylinder for $T/d = 2$.

In Table 2, the C_d for cylinder 1 (case II, $\alpha_1 = \alpha_2 = 45°$) is compared for various $T/d = 2$–4. The C_d is more or less constant at about 1.0, much smaller than that for case I (Table 1). Recall that C_d in Table 2 is computed based on the projected area $A = hd(\sin\alpha + \cos\alpha)$. By comparing the results for case I (Table 1) and case II (Table 2), it is observed that an average reduction of 42% in C_d occurs for case II ($T/d = 2$–4). This reduction is approximately equal to the increase in the projected surface, which is about 41%.

Table 2. Comparison of C_d of cylinder 1 for various configurations, i.e. SBS-WM (wall-mounted finite length side-by-side cylinders, case II ($\alpha_1 = \alpha_2 = 45°$); single-WM (single wall-mounted finite length cylinder), single-INF (infinite length single cylinder, $\alpha = 45°$).

Configuration	*Re*	AR	T/d	C_{d1}
SBS-WM (present)	8.1×10^4	7	2	1.04
SBS-WM (present)	8.1×10^4	7	3	1.02
SBS-WM (present)	8.1×10^4	7	4	0.98
Single-WM (Exp. [15])	7.3×10^4	7	–	1.06
Single-INF (Exp. [19])	9.98×10^3	–	–	1.6

As found in the previous section for the case I, the C_d for the case II (finite cylinder) is also smaller than that for infinite cylinders [19], see Table 2. This reduction for the case II is about 60% with respect to the single infinite cylinder ($Re = 9980$) [19] which is higher than that for the case I.

Figure 13 shows C_P on belts B and H of the cylinder 1 for the case III ($\alpha_1 = 0°$, $\alpha_2 = 45°$). Figure 13a illustrates that the results on the belt H are qualitatively similar to those observed in Fig. 8 for the case I ($\alpha_1 = \alpha_2 = 0°$) except for the side H_1–H_4. The side H_1–H_4 is located on the inner surface of the cylinder. The different variation on this side is due to the shape of the cylinder 1, which has a square and a diamond cross-section for cases I and II, respectively. A close similarity is also observed for the belt B in Figs. 9 and 13, although the difference on the side B_3–B_4 in the wake region is higher for the case I. As seen from Figs. 7, 9 and 13, the effect of T/d on the results is lower for the case III than for case I.

Table 3. The C_d of cylinder 1 for various T/d for case III ($\alpha_1 = 0°$, $\alpha_2 = 45°$). SBS-FL (wall-mounted finite length side-by-side cylinders); $Re = 8.1 \times 10^4$.

Configuration	*Re*	AR	T/d	C_d
SBS-WM (present)	8.1×10^4	7	2	1.43
SBS-WM (present)	8.1×10^4	7	3	1.38
SBS-WM (present)	8.1×10^4	7	4	1.44

a) b)

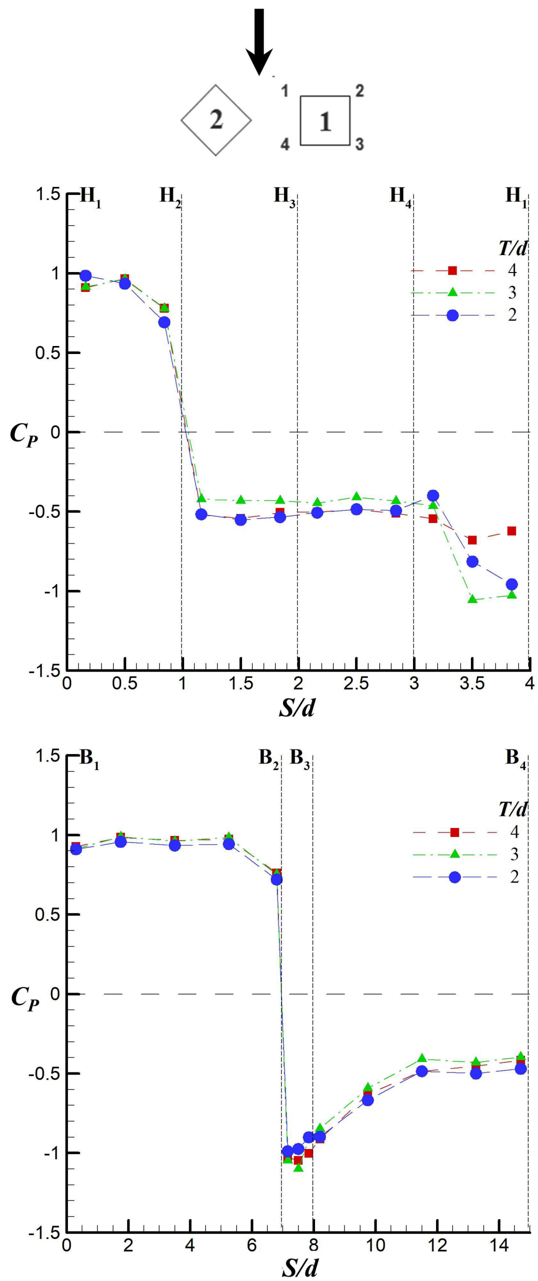

FIG. 13. Time-mean pressure coefficient variation along: a) belt H, b) belt B of cylinder 1 ($\alpha_1 = 0$), (case III, $\alpha_1 = 0°$, $\alpha_2 = 45°$), $Re = 8.1 \times 10^4$.

The C_d of the cylinder 1 for the case III ($\alpha_1 = 0°$, $\alpha_2 = 45°$) is presented in Table 3. The effect of T/d on C_d is not so much visible while the influence of

T/d is more noticeable for the case I especially for $T/d = 2$ and 3 (Table 1). For $T/d = 4$, C_d values for cases I and III are comparable. This shows that the flow interference effect on C_d becomes small in spite of the difference in the shape of the second cylinder for the two cases.

The results presented up to here are provided for $Re = 8.1 \times 10^4$ only, as the effect of Re ($= 5.9 \times 10^4$, 6.8×10^4, and 8.1×10^4) on the pressure results was not remarkable. A small variation in C_d is found when Re is increased, especially for a large T/d. As such, a small variation in C_d with Re is observed in Table 1 for a single wall-mounted cylinder, where $C_d = 1.41$ ($Re = 12\,800$, $AR = 6$) [12] and $C_d = 1.4$ ($Re = 73\,000$, $AR = 7$) [13]. See also [18] for an infinite cylinder.

4. Conclusions

With the variations in T/d and α, four flow structures are observed, i.e. the asymmetric flow, antiphase coupled-vortex shedding flow, leading-edge separated flow and wedge flow. While the former two flows are linked to the variation in T/d, the latter two associated with the individual cylinders are caused by the variation in α. The asymmetric and antiphase flows emerge at $T/d = 2$, 3 and 4, respectively, for both cases I and II, while only asymmetric flow appears for the case III. In the case of asymmetric flow, the gap flow is unstable, may switch from a side to the other for cases I and II, but it is stable for the case III, biased only toward the cylinder with $\alpha = 0\ ^\circ$. While both antiphase and inphase coupled-vortex shedding patterns materialize for two infinite side-by-side cylinders, only the antiphase flow was identified for two finite side-by-side cylinders; inphase flow was not observed for the latter where the tip vortices play a dominant role in the wake.

For the case I, the C_P is positive on the windward surfaces, at the mid-height, of the two cylinders. This is, however, not the case for cases II and III, where C_P varies significantly when $\alpha \neq 0°$. For asymmetric flow, the inner shear layers are close to the inner-side surfaces, resulting in a large variation in C_P on the inner-side surface. The pressure distributions near the floor and the free end are different from those near the mid-height due to the effect of tip and horseshoe vortices.

The total surface-averaged drag coefficient C_d for finite cylinders is lower than that for infinite cylinders while it has a nearly similar magnitude to that of a single wall-mounted cylinder, especially at a higher T/d. The trend of sectional drag coefficient C_D variation with z/d is different for $T/d = 3$ than for the other T/d. The C_D for the other T/d decreases with increasing z/d while it for $T/d = 3$ has a local maximum at $z/d = 5$. The C_D near the bottom is more sensitive to T/d than that near the top because the interaction of the base, horseshoe and

Kármán vortices between the cylinders is strong near the base of the cylinder. The C_D is smaller and larger near the tip and base, respectively, compared to C_d. The C_D at $0.5d$ below the mid-span can represent C_d.

References

1. M.M. Alam, Y. Zhou, X.W. Wang, *The wake of two side-by-side square cylinders*, Journal of Fluid Mechanics, **669**, 432–471, 2011.
2. M.M. Alam, Y. Zhou, *Intrinsic features of flow around two side-by-side square cylinders*, Physics of Fluids **25**, 085106, 2013
3. R.S. Sarode, S.L. Gai, C.K. Ramesh, *Flow around circular- and square-section models of finite height in a turbulent shear flow*, Journal of Wind Engineering and Industrial Aerodynamics, **8**, 223–230, 1981.
4. M.R. Rastan, A. Sohankar, M.M. Alam, *Low-Reynolds-number flow around a wall-mounted square cylinder: flow structures and onset of vortex shedding*, Physics of Fluids, **29**, 103601, 1–19, 2017.
5. H. Nakamura, T. Igarashi, T. Tsutsui, *Local heat transfer around a wall-mounted cube at 45° to flow in a turbulent boundary layer*, International Journal of Heat and Fluid Flow, **24**, 807–815, 2016.
6. A. Sohankar, M. Esfeh, H. Pourjafan, M.M. Alam, L. Wang, *Features of the flow over a finite length square prism on a wall at various incidence angles*, Wind and Structures, **26**, 317–329, 2018.
7. H. Bai, M.M. Alam, *Dependence of square cylinder wake on Reynolds number*, Physics of Fluids, **30**, 015102, 2018.
8. Q. Zheng, M.M. Alam, *Intrinsic features of flow past three square prisms in side-by-side arrangement*, Journal of Fluid Mechanics, **826**, 996–1033, 2017.
9. A. Sohankar, *Flow over bluff body from moderate to high Reynolds numbers using large eddy simulation*, Computer & Fluids, **35**, 1154–1168, 2006.
10. P.J. Pritchard, J.W. Mitchell, *Fox and McDonald's Introduction to Fluid Mechanics*, 8th ed., John Wiley & Sons, Madison, 2011.
11. R.F. Huang, B.H. Lina, S.C. Yen, *Time-averaged topological flow patterns and their influence on vortex shedding of a square cylinder in cross flow at incidence*, Journal of Fluids and Structures, **26**, 406–429, 2010.
12. A. Sohankar, S. Mohagheghian, A.A. Dehghan, M.D. Manshadi, *A smoke visualization study of the flow over a square cylinder at incidence and tandem square cylinders*, Journal of Visualization, **18**, 687–703, 2015.
13. M. Mirzaei, A. Sohankar, *Numerical study of convective heat transfer and fluid flow around two side by side square cylinders using k-ω-v2-f turbulence model*, International Journal of Heat and Mass Transfer, **49**, 1755–1769, 2013.
14. T. Uffinger, I. Ali, S. Becker, *Experimental and numerical investigations of the flow around three different wall-mounted cylinder geometries of finite length*, Journal of Wind Engineering and Industrial Aerodynamics, **119**, 13–27, 2013.

15. J.F. McClean, D. Sumner, *An experimental investigation of aspect ratio and incidence angle effects for the flow around surface-mounted finite-height square prisms*, Journal of Fluids Engineering, **136**, 081206–1, 2014.

16. H. Gang, K. T. Tse, K.C.S. Kwok, Y. Zhang, *Large eddy simulation of flow around an inclined finite square cylinder*, Journal of Wind Engineering and Industrial Aerodynamics, **146**, 172–184, 2015.

17. H. Gang, K. T. Tse, K.C.S. Kwok, Z.S. Chen, *Pressure measurements on inclined square prisms*, Wind and Structures, **21**, 4, 383–405, 2015.

18. S.C. Yen, J.H. Liu, *Wake flow behind two side-by-side square cylinders*, International Journal of Heat and Fluid Flow, **32**, 41–51, 2011.

19. S. Dutta, K. Muralidhar, P.K. Panigrahi, *Influence of the orientation of a square cylinder on the wake properties*, Experiments in Fluids, **34**, 16–23, 2003.

Received May 5, 2018; revised version August 18, 2018.